

Study of the Ni-rich multi-phase equilibria in Ni–Al–Pt alloys using the cluster/site approximation for the face-centered cubic phases

J. Zhu^a, C. Zhang^a, D. Ballard^b, P. Martin^b, J. Fournelle^c, W. Cao^d, Y.A. Chang^{a,*}

^a Department of Materials Science and Engineering, University of Wisconsin, Madison, WI 53706, USA

^b Air Force Research Laboratories, Wright-Patterson AFB, Dayton, OH 45433, USA

^c Department of Geology and Geophysics, University of Wisconsin, Madison, WI 53706, USA

^d CompuTherm LLC, 437 Yellowstone Dr. Suite 217, Madison, WI 53719, USA

Received 4 May 2009; received in revised form 28 August 2009; accepted 30 August 2009

Available online 30 September 2009

Abstract

The modified cluster/site approximation was used to describe the thermodynamics of the various face-centered cubic phases in Ni–Al–Pt, the Bragg–Williams approximation for the *B2* phase, and a modified regular solution formalism for the liquid phase. Coupled computational thermodynamics with key phase equilibrium measurements in the solid state, a thermodynamic description of this ternary for Ni contents higher than 50% was obtained based on these data and those given in the literature as well as the descriptions of its constituent binaries. Not only did the model-calculated solid-state phase equilibria agree with the measured data, the model-calculated liquidus projection is also able to account for the phases formed during solidification. In addition, the calculated chemical potentials or activities of Ni and Al are also in accord with the measured data as a function of temperature using mass spectrometry.

© 2009 Acta Materialia Inc. Published by Elsevier Ltd. All rights reserved.

Keywords: Nickel alloys; Cluster/site approximation; Thermodynamics; CALPHAD

1. Introduction

Improvement of the oxidation resistance of Ni-base superalloys at high temperatures by alloying with Pt [1] motivates an understanding of the multi-phase equilibria between the Ni-rich face-centered cubic fcc-*A1*–(Ni,Al,Pt) phase denoted as γ and the ordered intermetallic *L1*₂–(Ni,Pt)₃Al phase denoted as γ' . The two-phase equilibrium of γ' and β -*B2*–(Ni,Pt)Al is also of importance since β –(Ni,Pt)Al is used as a bond coat material for traditional Ni-base superalloy airfoils [1]. In the present study, we adopt the methodology using computational thermodynamics to first identify key alloys for experimentation; the results obtained enables one to rapidly obtain a thermodynamic description of the system in question such as Ni–Al–Pt in the present study [2–4]. The term thermody-

namic description denotes that the thermodynamic model parameters for all the phases in question are known as a function of composition and temperature at a constant pressure of 1 bar. In other words, a preliminary thermodynamic description of Ni–Al–Pt is obtained from those of its three constituent binaries, Ni–Al [5], Ni–Pt [6] and Al–Pt [6] as well as diffusion couple data reported by Gleeson et al. [1,7] in Ni–Al–Pt. We selected fourteen alloys for experimentation: four in the two-phase equilibrium of γ and γ' for study at 1433 K, five in the same two-phase equilibrium for study at 1523 K and five in the two-phase equilibrium of γ' and β for study at 1523 K. In this study, the modified cluster/site approximation (CSA) is used to describe the thermodynamics of the disordered fcc-*A1* solution phase and the various ordered intermetallic phases such as the *L1*₂ and *L1*₀ phases [8–19]. The β phase, treated as a triple-defect phase [20,21], is described by the compound energy formalism based on the Bragg–Williams approximation [22–26], and the liquid phase by a modified

* Corresponding author. Tel.: +1 608 262 0389; fax: +1 608 262 8353.
E-mail address: chang@engr.wisc.edu (Y.A. Chang).

regular solution formalism. In the following we will present thermodynamic models (Section 2), experimental methods and results (Section 3), discussion of the modeling and experimental results (Section 4), and conclusions (Section 5).

2. Thermodynamic models

2.1. The CSA

The CSA is an adaption of the generalized quasi-chemical method which was first introduced by Fowler [27] for treating atom/molecule equilibria in gases and subsequently applied to clusters in solid solutions by Yang and Li [8–11], taking both long-range order (LRO) and short-range order (SRO) into consideration. Later, Oates and Wenzl realized that the Yang–Li model, which they termed the cluster/site approximation, had big advantages over the cluster variation method (CVM) for its application to multi-component systems in the sense that the independent variables in the CSA are the point probabilities rather than the much more numerous cluster probabilities in the CVM [28]. More recently, Oates et al. modified the CSA for application to real alloy systems by using the ζ , the number of clusters per site, as an adjustable parameter and demonstrated that the modified CSA gave fcc prototype phase diagrams comparable with those derived either from MC simulations or from using the CVM in the tetrahedron approximation [12].

Since the clusters in the CSA must be energetically non-interfering, i.e. they are permitted to share only corners but not faces or edges, the configurational entropy thus involves only the cluster entropy and the single-site entropy. Accordingly, there are only two terms in the entropy expression. The entropy per site S_m can be written as

$$S_m = \zeta S_n - (n\zeta - 1)S_1 \quad (1)$$

where ζ is the number of energetically non-interfering clusters per site. In the nearest-neighbor pairwise approximation, as was used by Yang and Li, $\zeta = z/2p$ with z being the nearest-neighbor coordination number and p the number of nearest-neighbor pairs in the cluster of size n . In the modified CSA, as mentioned earlier, ζ is treated as an adjustable parameter. The dimensionless cluster and site entropies, S_n and S_1 , are given by $S_n = -\sum_i Z_i \ln Z_i$ and $S_1 = -\sum_i X_i \ln X_i$, respectively, where Z_i is the cluster probability and X_i is the point probability.

The molar free energy in the modified CSA, F_m , for a C -component system is [12,14]

$$\frac{F_m}{RT} = \zeta \left(\sum_P^{C-1} \sum_{i=1}^n y_P^i \mu_P^i - \ln \lambda \right) - (n\zeta - 1) \left(\sum_P^C \sum_{i=1}^n f_i y_P^i \ln y_P^i \right) \quad (2)$$

where f_i is the fraction of the sublattice type i , and y_P^i the sublattice mole fraction of component P on sublattice i .

The μ_P^i 's are Lagrangian multipliers arising from the mass balance constraints and are related to the species chemical potentials of the atoms on the sublattice i . The cluster partition function, λ , is expressed in terms of the cluster energies and the μ_P^i as given below:

$$\lambda = \sum_{j=1}^{C^n} \exp \left[\left(\sum_P^{C-1} \sum_{i=1}^n \mu_P^i \right)_j - \varepsilon_j \right] \quad (3)$$

For the application of the modified CSA to real multi-component fcc alloys, the free energies are taken to consist of two terms, the configuration-dependent term, F_{CD} and the configuration-independent term F_{CI} , [28,15] as given below:

$$F_m = F_{CD} + F_{CI} \quad (4)$$

In this paper, the configuration-dependent term, F_{CD} , represented by Eqs. (2) and (3), is a function of y_P^i , and configuration-independent term, F_{CI} , is a function of x_P and represented by the Redlich–Kister equation [29].

$$F_{CI} = \sum_{P,Q} x_P x_Q \sum_{i=0}^n L_i (x_P - x_Q)^i \quad (5)$$

where P, Q are the component elements.

2.2. The β -B2 phase

The β phase in binary Al–Pt is not stable. Jiang et al. [30,31] performed first-principles calculations and found that Pt always has a predominate preference for the Ni sublattice and the amount of Pt on the Al sublattice is small even at high temperatures for both β -(Ni,Pt)Al phase and γ' -(Ni,Pt)₃Al phase. Accordingly, the ternary β phase can be described as (Al,Ni,Pt)₁(Ni,Pt,Va)₁. The Gibbs energy per mole of formula unit, i.e. $2 - y_{Va}'$ mole of atoms, is expressed as follows:

$$G_m = \sum_i \sum_j y_i' y_j'' G_{ij}^{B2} + RT \left(\sum_i y_i' \ln y_i' + \sum_j y_j'' \ln y_j'' \right) + \sum_i \sum_k \sum_j y_i' y_k' y_j'' L_{i,k;j}^{B2} + \sum_i \sum_j \sum_l y_i' y_j' y_l'' L_{i,j;l}^{B2} \quad (6)$$

The symbols $i, k = \text{Al, Ni, Pt}$ and $j, l = \text{Ni, Pt, Va}$ respectively with Va denoting vacancy.

2.3. The liquid phase

The Gibbs energy of the liquid phase is represented by the following equation in terms of one mole of atoms:

$$G_m^{Liq} = \sum_i x_i^0 G_i^{Liq} + RT \sum_i x_i \ln x_i + x_s G_m^{Liq} \quad (7)$$

The symbol x_i denotes the mole fraction of the component “ i ” ($i = \text{Al, Ni, Pt}$). The first term on the right-hand side of the equation is the reference term and thermodynamic values $^0 G_i^{Liq}$ are taken from Dinsdale [32]. The second term on the right-hand side of this equation is the

ideal mixing term, and the last term, the excess free energy, is again represented by the Redlich–Kister equation [29] as given below:

$$\Delta^{\text{xs}} G_m^{\text{Liq}} = \sum_i \sum_{j>i} \sum_k x_i x_j L_{i,j}^{\text{Liq},k} (x_i - x_j)^k + x_{\text{Al}} x_{\text{Ni}} x_{\text{Pt}} \sum_{i=\text{Al}, \text{Ni}, \text{Pt}} x_i L_{\text{Al}, \text{Ni}, \text{Pt}}^i \quad (8)$$

The binary interaction parameters $L_{i,j}^{\text{Liq}}$ are taken from the constituent binaries and the ternary parameters $L_{\text{Al}, \text{Ni}, \text{Pt}}^i$ are obtained by optimization in terms of experimental data in the ternary system.

3. Experimental methods and results

All thermodynamic calculations and parameter optimizations were carried out using the Pandat software [33] and PanOptimizer [34]. On the basis of the calculated 1433 K isotherm using this preliminary description, four alloys containing γ and γ' , designated as sample nos. 1–4, were prepared. A fifth alloy in the single-phase β phase field, designated as sample no. “m”, was also prepared. The overall compositions of these alloys are in the $\gamma + \gamma'$ two-phase field and given in Table 1. The plan is to use the first four samples to determine the compositions of the co-existing γ and γ' phases or the tie lines between γ and γ' at 1433 K. The five alloys were prepared at the Air Force Research Laboratory, Materials and Manufacturing Directorate at the Wright–Patterson AFB, Dayton, OH. Thirty gram “finger” buttons were arc melted five times in high-purity argon gas at 381 mm Hg (15 in Hg, 0.5 bar). These buttons were then remelted three additional times in an argon backfilled Crystallox furnace with a positive pressure of 2–4 psig to maximize mixing. The metals used were 99.95% pure Ni shot, 99.98% pure Al pellets, and 99.998% pure Pt sponge (all compositions are given in at.%, unless otherwise stated). Each of the melted samples was first annealed at 1523 K for 100 h, then at

1558 K for 96 h and gas-quenched, and annealed at 1623 K for 170 h. The highest annealing temperature was selected based on the calculated melting temperatures of these samples using the preliminary description. Since none of the samples encountered melting during the heat treatment at the highest temperature, we were led to believe that the preliminary thermodynamic description obtained is already quite good.

In addition to samples nos. 1–4, given in Table 1, ten additional samples were prepared at UW-Madison using the single-phase β sample denoted as “m” given in Table 1 as a master alloy. These alloys were prepared by arc melting and by adding appropriate amounts of 99.99% Ni and 99.995% Al. Five of these samples, i.e. nos. 5–9, were used to determine the tie lines in the same $\gamma + \gamma'$ two-phase field and the other five, i.e. nos. 10–14, the tie lines in the $\gamma' + \beta$ two-phase field all at 1523 K. The overall compositions of these alloys are also summarized in Table 1. All the alloy samples were wrapped with Ta foil for isothermal annealing: sample nos. 1–4 at 1433 K for 30 days, 5–9 and 10–14 at 1523 K for 30 days. In addition, samples nos. 1, 2, 12, 13 and 14 in the as-cast condition were also characterized to identify the primary phases of solidification and the subsequent microstructures.

The annealed and solidified samples were carefully ground and polished to get scratch-free surfaces. The microstructure of each sample was examined using a JEOL JSM6100 scanning electron microscope (SEM) operated at 15 kV in the backscattered electron (BSE) imaging mode equipped with Noran energy-dispersive spectrometry (EDS) system. X-ray diffraction (XRD) analysis was performed using a STOE Bragg–Brentano diffractometer to identify the crystal structures of these phases. The compositions of the co-existing phases in the $\gamma + \gamma'$ and $\gamma' + \beta$ phases were determined using wavelength dispersive X-ray spectrometry (WDS) electron probe microanalysis (EPMA); the specific instrument used is CAMECA SX51 located in the Department of Geology and Geophysics, UW-Madison. Operating conditions were 20 kV, 30 nA Faraday cup current. It is noteworthy to point out that an extensive effort was expended as given below in order to obtain accurate EPMA results for the Ni–Al–Pt alloys.

Electron probe microanalysis (EPMA) is a well established technique used to quantitatively characterize many materials at the micron scale, and is regarded as a mature, robust procedure which yields information of high accuracy and precision. Early in its development, Castaing [35] presented a theory and a procedure that has remained essentially unchanged: EPMA uses standards to determine k -ratios (intensity of unknown X-ray line divided by same of the standard), which are then modified by a matrix correction to yield the composition of the unknown. This matrix correction relies on a physical model that provides the basis for correcting the measured raw X-ray intensities for actual modifications in generation and absorption in the unknown matrix, relative to pure element standards. These corrections are known as the ZAF or the phi–

Table 1
Overall compositions of selected alloys.

Alloy no.	Composition (at.%)			Phases involved	Annealing temperature (K)
	Pt	Al	Ni		
1	9.70	19.00	Bal	$\gamma + \gamma'$	1433
2	16.90	18.60	Bal	$\gamma + \gamma'$	1433
3	22.40	18.30	Bal	$\gamma + \gamma'$	1433
4	28.90	17.60	Bal	$\gamma + \gamma'$	1433
5	5.41	19.61	Bal	$\gamma + \gamma'$	1523
6	10.88	18.04	Bal	$\gamma + \gamma'$	1523
7	15.27	17.98	Bal	$\gamma + \gamma'$	1523
8	18.88	17.01	Bal	$\gamma + \gamma'$	1523
9	23.36	17.82	Bal	$\gamma + \gamma'$	1523
10	4.76	28.57	Bal	$\gamma' + \beta$	1523
11	9.15	31.26	Bal	$\gamma' + \beta$	1523
12	12.41	31.76	Bal	$\gamma' + \beta$	1523
13	13.61	31.19	Bal	$\gamma' + \beta$	1523
14	15.16	29.27	Bal	$\gamma' + \beta$	1523
m	25.20	31.90	Bal	–	–

rho-Z procedures, and there are several possible versions. Herein lies a potential problem for certain materials, such as the ones under consideration here: the matrix correction was not accurately developed for compounds with a wide range of atomic numbers using pure element analytical standards. For example, Armstrong [36] and Carpenter [37] reported an issue at Cal Tech years ago for a Si–Ir unknown sample. Using pure Si and pure Ir as standards, significantly different final results (Si55Ir45 vs. Si50Ir50) became possible for a single unknown material depending upon which one of the eight different matrix correction schemes was used with the pure element standards. The problem appears to have several components: (1) incorrect mean atomic number estimation for the Z (atomic number) correction of phases with disparate Z values [38], (2) failure to include continuum fluorescence which can be a problem for high atomic number standards (e.g. Ir, Pt), and to a possibly smaller extent, and (3) choice of the best mass absorption coefficients. Potentially there is also (4) the possibility for peak shifts in low-energy X-ray lines (e.g. Al Ka, Ni La, etc.), though this is easy to determine and correct. The effect of different matrix corrections on our EPMA measurement is demonstrated when ten different matrix correction algorithms and factors are used to correct the same *k*-ratio for X-ray intensities measured using the UW-Madison Cameca SX51 electron probe. And different values are calculated when Pt La is used rather than Pt Ma. Table 2 lists the data for alloy Ni–24.2Al–31.1Pt (this alloy was used to determine the correction factor and not to obtain the current thermodynamic description due to its high Pt concentration while we were focusing on the Ni-rich corner), first using pure Pt metal and NiAl intermetallic compound as the standards. In addition to the wide range of possible values for each element in this unknown phase, the analytical totals outside of the acceptable range of 99–101 wt.% suggest a significant inaccuracy in the results.

It is essential in EPMA to consider non-normalized analytical results, for totals <99 and >101 generally indicate that an analytical problem exists. And with the distinct different values for the same element for one measurement, it is difficult to know which matrix correction is most appropriate. After additional testing and discussion, the alloy no. *m* (Ni–31.9Al–25.2Pt) was selected as the standard based on the fact that there is only one homogenized phase in the microstructure. This sample was sent out for independent chemical analysis, and it is also modeled using the PENEPMA Monte Carlo model, see below. It was used as the analytical standard assuming that the nominal starting material composition is correct. This was the approach used by Armstrong and Carpenter in determining the actual SiIr phase composition. When using this approach, there is much less extrapolating from extreme end member elemental compositions, and the matrix corrections begin to converge upon a tighter compositional range. Using this experimental single phase as the standard, significantly different results were obtained

Table 2

Comparison of EPMA data on alloy Ni–24.2Al–31.1Pt (Ni–6.99Al–64.9Pt in wt.%) using different standards under ten different matrix correction algorithms and factors.

Standard	Element	Concentration (wt.%)	
		Pt La	Pt Ma
NiAl	Al	6.28–8.63	6.24–8.57
NiAl	Ni	23.44–27.25	23.40–27.18
Pt metal	Pt	64.72–66.39	64.23–68.03
	Total	95.26–98.88	96.64–102.29
Alloy no. <i>m</i>	Al	6.54–6.72	6.53–6.71
Alloy no. <i>m</i>	Ni	27.92–28.55	27.88–28.52
Alloy no. <i>m</i>	Pt	64.92–65.55	65.74–66.70
	Total	99.38–100.50	100.16–100.60

for the alloy Ni–24.2Al–31.1Pt examined above as listed in Table 2.

We then see that the matrix corrected values converge regardless of which matrix correction was used. Using the original set of standards (NiAl and Pt), and the average of all the different possible results using the different matrix corrections, Al is 12% relative (<1 wt.% absolute) too high, and Ni is 10% relative (3 wt.% absolute) too low. On average the Pt values do not change much. The large error in the Ni measurement appears to be due to the strong secondary fluorescence of the Ni Ka (edge 8.31 keV) by the Pt La (9.44 keV) which is not correctly accounted for in the matrix correction. It is not surprising, given that this effect has been ignored in most prior matrix corrections due to its complexity. An additional test was made using the PENEPMA Monte Carlo simulation software. This approach uses a physical model (created for simulating radiation effects) that does not involve the approximations present in the EPMA matrix corrections. Some Monte Carlo modeling suggests that the last data (using Pt Ma) is more correct for the Pt value, as the continuum contribution (and error) is minor compared to the Pt La. Our conclusion to use an intermediate Ni–Al–Pt single-phase standard provides the most accurate EPMA data, once we have verified its composition. We thus conclude that the accuracy of the EPMA to analyze the compositions of the Ni–Al–Pt alloys is within 1 at.%.

In the following, we present the experimental results obtained and make comparison between the model-calculated phase equilibria with the measured values when appropriate. As given in Fig. 1a, the microstructure of sample no. 3 with 18.3%Al and 22.4%Pt annealed at 1433 K for 30 days shows the existence of two phases. In view of the different densities of these two phases, the dark phase must be γ and the light phase γ' . The XRD patterns of this sample shown in Fig. 1b show conclusively one phase is fcc-Al and the other $L1_2$. The lattice parameters of γ and γ' are 0.3631 and 0.3699 nm, respectively. In addition, the microstructure also exhibits the precipitation of γ' within the γ phase as expected in view of the lower solubilities of Al in the γ phase at lower temperature according to the calculated solidus using the thermodynamic description!

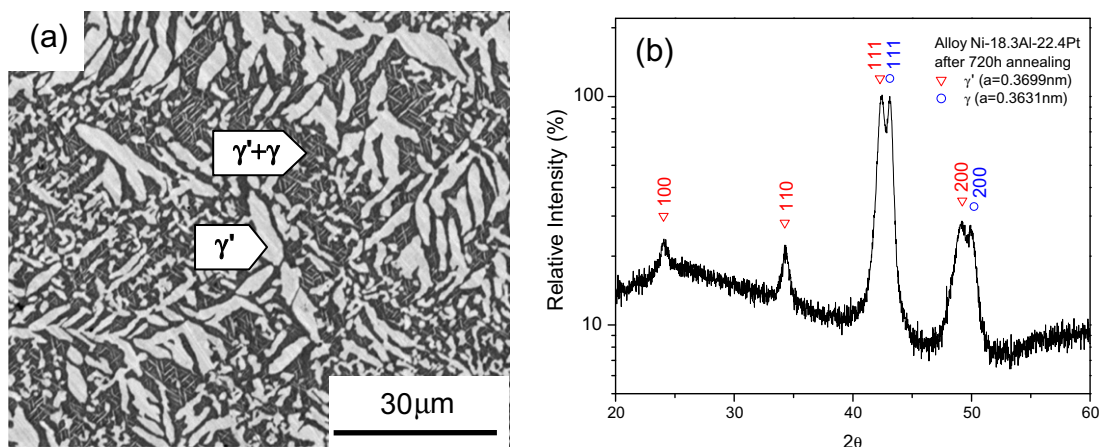


Fig. 1. (a) BSE image and (b) XRD pattern for alloy #3 (Ni-18.3Al-22.4Pt).

The BSE image of sample no. 7 with 18.0%Al and 15.3%Pt, annealed at 1523 K for 30 days, as given in Fig. 2a, shows the alloy consists of γ and γ' . The microstructure is basically similar to that shown in Fig. 1a with the exception that the sizes of the two phases are larger due to higher temperature annealing. Note that the samples nos. 1–4 were originally sealed in a quartz tube in an ultra-high-purity argon atmosphere (99.998% Ar) before being annealed at elevated temperatures, and water quenched after annealing, which resulted in numerous precipitates. The other Ta-wrapped and not encapsulated samples nos. 5–9 and 10–14 were annealed in an ultrahigh-purity argon atmosphere and directly quenched into water after annealing to achieve faster cooling rate. Precipitates were barely observed in the microstructures of these samples.

The BSE image of sample no. 13, with 31.19%Al and 13.61%Pt, annealed at 1523 K for 30 days, is given in Fig. 2b. There are two distinct phases which coexist. Phase identification using EPMA and SEM/EDS indicates that the dark phase is γ' and the bright one is β phase.

4. Discussion of the modeling and experimental results

The data obtained in the present study are used to obtain an improved thermodynamic description of the ter-

nary Ni–Al–Pt system. The model parameters of the various phases are given in Table 3. The calculated isothermal sections at 1433 K and 1523 K using this description are shown in Figs. 3 and 4. It is noteworthy to point out that the phase boundaries of the $\gamma + \gamma'$ and $\gamma' + \beta$ calculated using the final description, i.e. using the model parameters given in Table 3, differ only slightly from those calculated using the preliminary description. The difference between the calculated phase boundaries using these two descriptions is less than 0.5% for the $\gamma + \gamma'$ boundaries and less than 1% for the $\gamma' + \beta$ phase boundaries. This is due primarily to the fact that the parameters of the CSA model for the fcc-Al and the $L1_2$ phases are only slightly different. Within the uncertainties of the measured compositions of the individual phases as noted in Section 3, the agreement between the model-calculated and experimentally determined phase boundaries is reasonable. It is worth noting that there is also a three-phase equilibrium of $\gamma + \gamma' + 2\ 1\ 1$ in the 1433 K isotherm toward the Pt-rich side of the diagram given in Fig. 3. The phase designated as α by Gleeson et al. [1] and Hayashi et al. [7] is referred to as $2\ 1\ 1$. Since the Pt composition of the $2\ 1\ 1$ phase is higher than 50%Pt, it does not appear in the isotherm given in Fig. 3. Had we extended the compositions to higher Pt contents, we would have a tie triangle in this

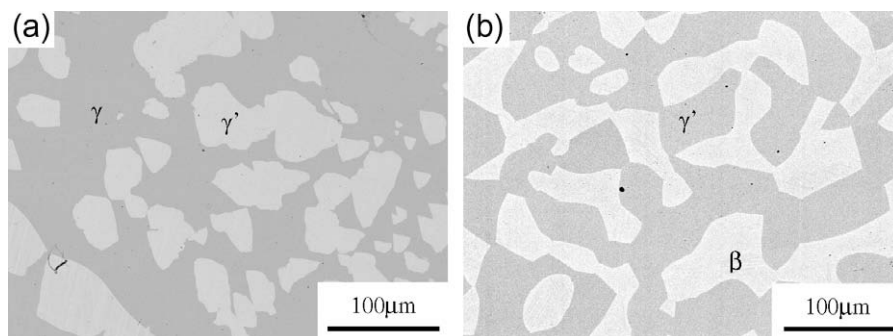


Fig. 2. BSE images show the microstructure of alloys in different two-phase regions: (a) alloy #7 (Ni-17.98Al-15.27Pt) in the $\gamma + \gamma'$ two-phase region and (b) alloy #13 (Ni-31.19Al-13.61Pt) in the $\gamma' + \beta$ two-phase region.

Table 3
Thermodynamic properties of the phases (J mol^{-1}).

Phase name	Model	Parameters
Liquid (L)	Substitutional solution (Al,Ni,Pt) ₁	${}^0L_{\text{Al,Pt}} = -330,527 + 16.97\text{ T}$ ${}^1L_{\text{Al,Pt}} = 48,317$ ${}^2L_{\text{Al,Pt}} = 24,716 + 25\text{ T}$ ${}^0L_{\text{Ni,Pt}} = -45,300$ $L_{\text{Al,Ni,Pt}}^{\text{Al}} = -130,000$ $L_{\text{Al,Ni,Pt}}^{\text{Ni}} = -60,000$ $L_{\text{Al,Ni,Pt}}^{\text{Pt}} = -150,000$
B2 (β)	Compound energy (Al,Ni,Pt) ₁ (Ni,Pt,Va) ₁	${}^0L_{\text{Al,Pt}} - {}^0G_{\text{Al}}^{\text{bcc}} - {}^0G_{\text{Pt}}^{\text{bcc}} = -207,083 + 17.213\text{ T}$ ${}^0L_{\text{Pt,Pt}} - 2{}^0G_{\text{Pt}}^{\text{bcc}} = 0$ ${}^0L_{\text{Pt,Va}} - {}^0G_{\text{Pt}}^{\text{bcc}} = 50,000$ ${}^0L_{\text{Ni,Pt}} - {}^0G_{\text{Ni}}^{\text{bcc}} - {}^0G_{\text{Pt}}^{\text{bcc}} = -22,000$ ${}^0L_{\text{Pt,Ni}} - {}^0G_{\text{Ni}}^{\text{bcc}} - {}^0G_{\text{Pt}}^{\text{bcc}} = -22,000$ ${}^0L_{\text{Al,Pt}*} = -155,000$ ${}^0L_{\text{Ni,Pt}*} = -45,000$
fcc	CSA (Al,Ni,Pt) _{0.25} (Al,Ni,Pt) _{0.25} (Al,Ni,Pt) _{0.25} (Al,Ni,Pt) _{0.25}	$\zeta = 1.35$ $\varepsilon_{\text{Al}_2\text{Pt}_2} = -21,500$ $\varepsilon_{\text{Al}_3\text{Pt}} = -15,000$ $\varepsilon_{\text{AlPt}_3} = -23,160 + 0.5\text{ T}$ $\varepsilon_{\text{Ni}_2\text{Pt}} = \varepsilon_{\text{NiPt}_2} = -7408$ $\varepsilon_{\text{Ni}_2\text{Pt}_2} = -7602$ ${}^0L_{\text{Ni,Pt}} = 63,865 - 3.6\text{ T}$ ${}^1L_{\text{Ni,Pt}} = -1000$ ${}^2L_{\text{Ni,Pt}} = -8000$ $\varepsilon_{\text{AlAlNiPt}}^{\text{E}} = 0$ $\varepsilon_{\text{AlNiNiPt}}^{\text{E}} = -3000$ $\varepsilon_{\text{AlNiPtPt}}^{\text{E}} = -7000$

Note: the cluster energy ε of $ijkl$ type can be expressed by pair exchange energies ε_{ij} and ternary interaction energy $\varepsilon_{ijkl}^{\text{E}}$, $\varepsilon_{ijkl} = \varepsilon_{ij} + \varepsilon_{ik} + \varepsilon_{il} + \varepsilon_{jk} + \varepsilon_{jl} + \varepsilon_{kl} + \varepsilon_{ijkl}^{\text{E}}$.

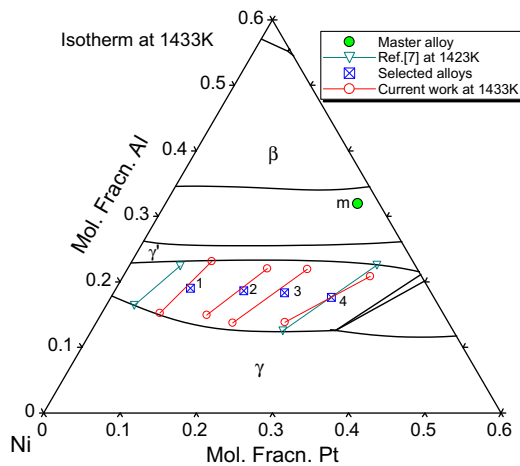


Fig. 3. Ni–Al–Pt isothermal section in the Ni-rich corner at 1433 K with experimental data.

isotherm. Instead we only observe two Pt-rich tie lines that emanate from the γ phase but do not intersect to the α phase! Since the current study focuses on the Ni-rich

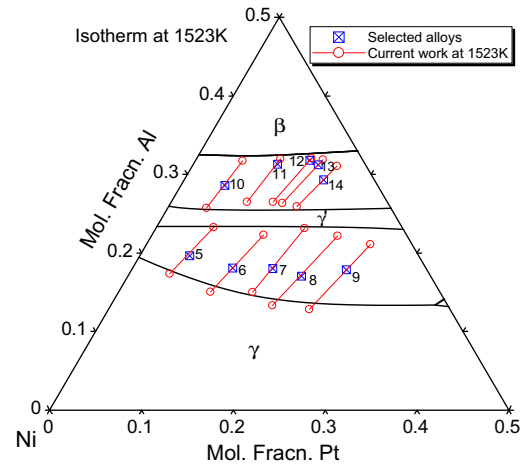


Fig. 4. Ni–Al–Pt isothermal section in the Ni-rich corner at 1523 K with experimental data.

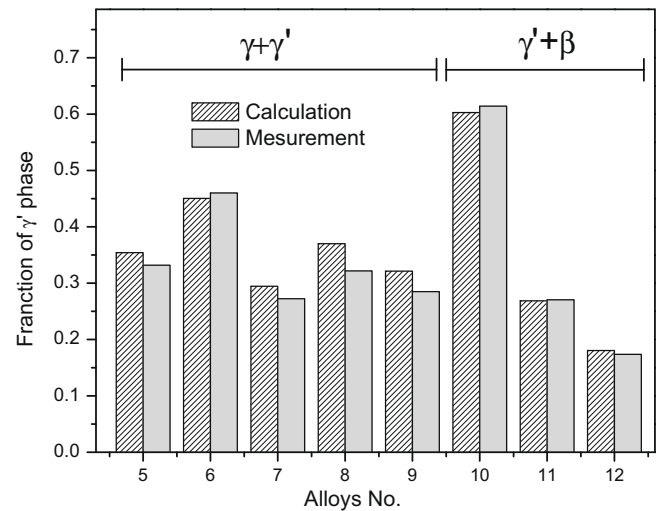


Fig. 5. Comparison between the model-calculated and experimentally measured γ' phase fraction in the $\gamma + \gamma'$ and $\gamma' + \beta$ two-phase regions. *Experimental measurements were obtained via image analysis.

multi-phase equilibria, we do not discuss the stability of the α phase. Fig. 5 presents another comparison of the model-calculated phase fractions of the γ' phase with those determined experimentally in the $\gamma + \gamma'$ and $\gamma' + \beta$ two-phase fields. The measured fractions of the γ' phase were obtained from image analysis. Based on our previous experience, the uncertainty of image analysis is within 1%. As shown in Fig. 5, the model-calculated γ' phase fractions are in good agreement with the results from image analysis.

As noted earlier, the thermodynamic description was obtained in terms of those of the constituent binaries and the phase boundaries obtained in this study at two temperatures and the diffusion couple results of Gleeson et al. [1,7]. Since the measured activity data [39] were not used in obtaining this description, it is interesting to compare the thermodynamic model-calculated activity values with the experimentally measured ones. As shown in Fig. 6a

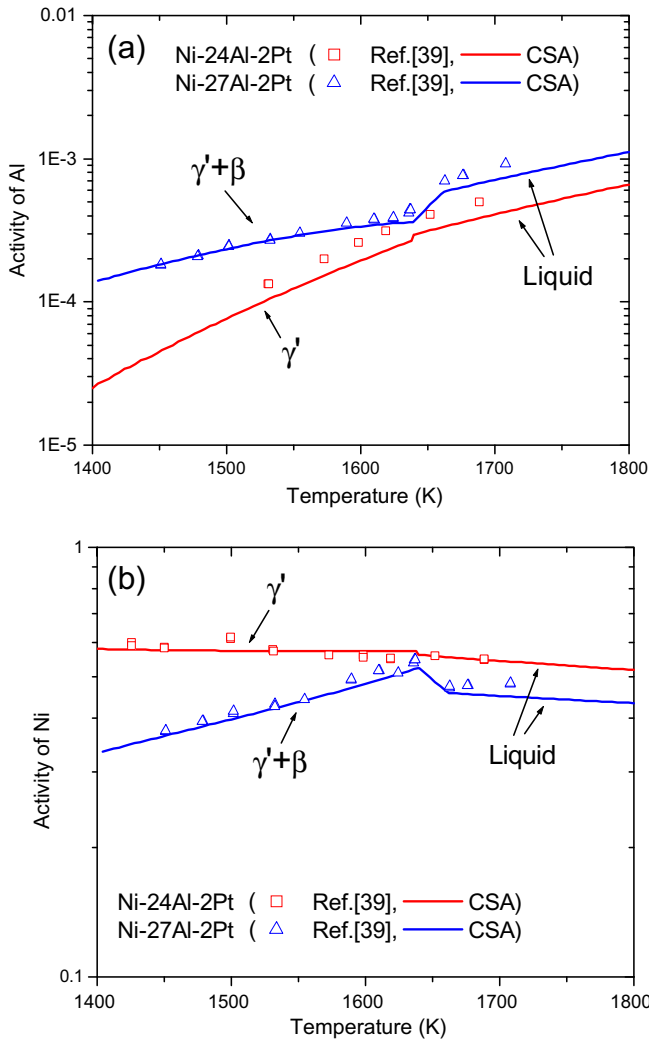


Fig. 6. The CSA-calculated activities of (a) Al and (b) Ni with the experimentally measured activities [39] for alloy Ni-24Al-2Pt and Ni-27Al-2Pt.

and b, the model-calculated activity values for Al and Ni are in agreement with the measured data [39] for the alloy containing 24% Al and 2% Pt as well as that containing 27% Al and 2% Pt as a function of temperature from $T = 1400$ – 1800 K. It is indeed surprising to see the close

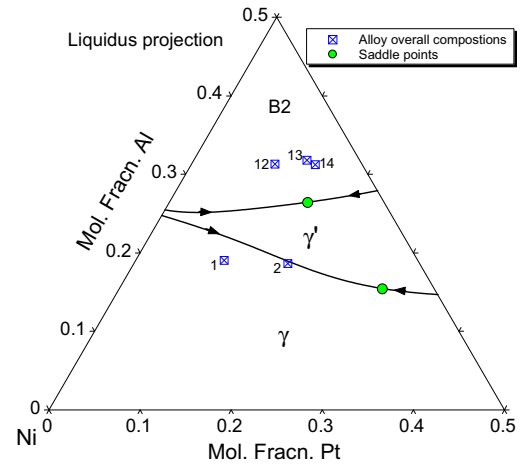


Fig. 7. Calculated liquidus projection of the Ni–Al–Pt system in the Ni-rich region with the overall compositions of the as-cast alloys.

agreement between the calculated activities of Al and Ni of the γ' phase over a wide temperature range from the solid state to the liquid state as well as those for the $\gamma' + \beta$ mixture also from the solid state to the liquid state. It is also encouraging that the calculated activities through the $S + L$ two-phase region capture in detail the variation of the measured activities as a function of temperature! This agreement suggests that the calculated melting temperatures of Ni–Al–Pt alloys may be indeed quite good. This is encouraging since no measured melting points for any of ternary alloys were available to be used to obtain the thermodynamic description.

We will next examine the calculated liquidus projection of Ni–Al–Pt in the Ni-rich corner shown in Fig. 7. There are two monovariant liquidus lines, one in equilibrium with γ and γ' and the other with γ' and β . It is evident that the temperature of the Al-poorer monovariant liquidus line emanates from the Ni–Al binary peritectic, i.e. $L + \gamma = \gamma'$, to the ternary region and the solidification ends at the minimum denoted as a solid circle. In a similar manner, the Al-richer monovariant liquidus line emanates from the Ni–Al binary eutectic, i.e. $L = \gamma' + \beta$, to the ternary region and the solidification ends also at the minimum temperature denoted as a solid circle. We examined the

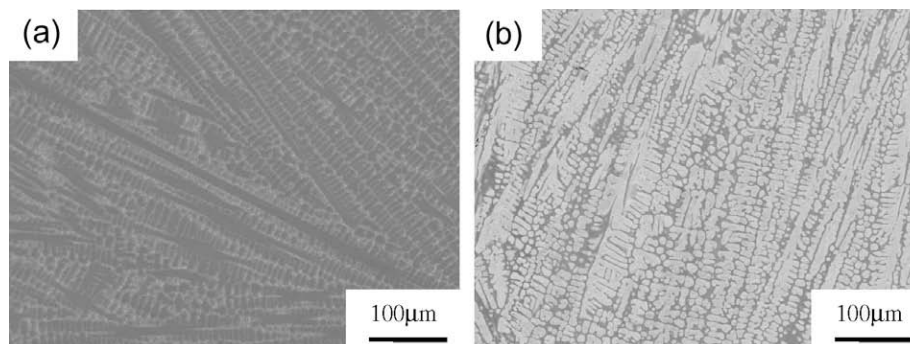


Fig. 8. BSE images of as-cast microstructures of alloy #1 and #12: (a) alloy #1 (Ni-19Al-9.7Pt): γ (dark phase) and γ' (bright phase); (b) alloy #12 (Ni-31.74Al-12.41Pt): B2 (bright phase) and γ' (dark phase).

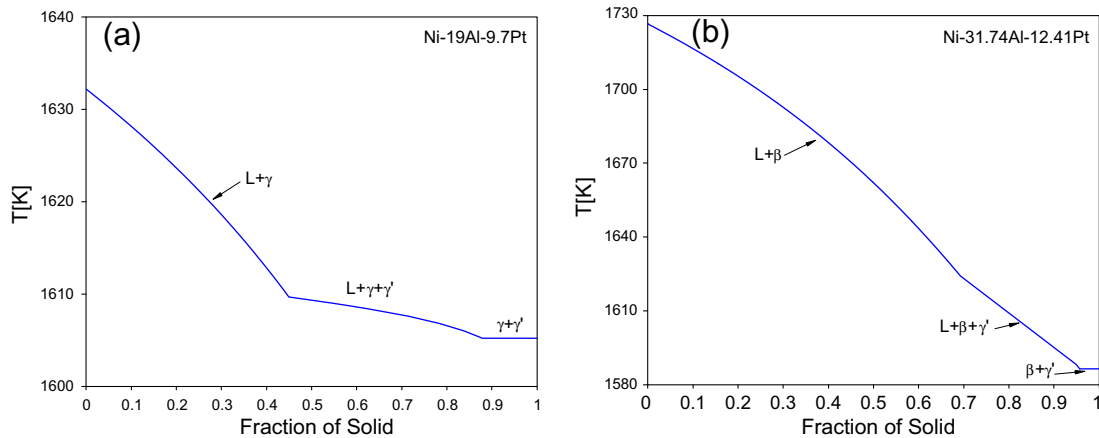


Fig. 9. The Scheil calculated solidification paths of (a) alloy #1 and (b) alloy #12.

microstructures of five alloys, i.e. samples no. 1, 2, 12–14 cast in a water-cooled copper mold in an arc melter. The microstructures of samples nos. 1 and 2 show the primary phase solidification of γ followed by a two-phase structure of γ/γ' . Those of samples 12–14 show the primary phase solidification of β followed by a two-phase structure of β/γ' . Typical microstructures of samples no. 1 and 12 are shown in Fig. 8a and b. The microstructures of these five solidified samples are all consistent with the calculated liquidus projection. Using the Scheil model [40], which is based on the assumptions that local equilibrium prevails at the liquid/solid interfaces, no diffusion takes place in the solids and infinitely fast diffusion occurs in the liquid, we calculated the solidification paths of the samples no. 1 and 12 (as shown in Fig. 9). According to our calculation in Fig. 9a, the sequence of phase formation of sample no. 1 consists of multiple stages: $L \rightarrow L + \gamma \rightarrow L + \gamma + \gamma' \rightarrow \gamma + \gamma'$. The calculated fraction of the primary γ phase is about 42%, which is consistent with the experimental observation in Fig. 8a. The solidification path of sample no. 12 is: $L \rightarrow L + \beta \rightarrow L + \beta + \gamma' \rightarrow \beta + \gamma'$. The calculated primary β phase fraction is 69% and it also agrees well with the experimental results shown in Fig. 8b.

5. Conclusion

A thermodynamic description of Ni–Al–Pt for Ni-content higher than 50% was obtained in terms of multi-phase equilibria involving γ and γ' as well as γ' and β in addition to constituent binary descriptions. The modified CSA successfully described the phase equilibrium between the disordered γ and the ordered γ' phase as expected. The calculated phase diagrams using this description agree with the experimental data within the uncertainties of the measured values and the calculations. In spite of the fact that there is no melting information available for any of the Ni–Al–Pt alloys, the model-calculated liquidus projection is able to account for the solidification paths of several alloys investigated in this study. By the same token the thermodynamic description was developed using only

known phase equilibria as noted above, the model-calculated thermodynamic activities of Ni and Al for a γ' alloy and a $(\gamma' + \beta)$ mixture are in agreement with the measured data from the solid state to the liquid region using mass spectrometry. The calculated activities through the $S + L$ two-phase region are in surprising accord with the temperature variation of the measured activities. We can thus conclude that the description obtained can be used to have an understanding of the phase stabilities of the Ni–Al–Pt alloys for contents more than 50% Ni.

Acknowledgements

The authors wish to thank the Air Force of Scientific Research for financial support through Grant No. F49550-06-1-0229.

References

- [1] Gleeson B, Wang W, Hayashi S, Sorelet DJ. *Mater Sci Forum* 2004;461–464:213.
- [2] Yang Y, Chang YA, Tan L, Cao W. *Acta Mater* 2005;53:1711.
- [3] Cao H, Zhu J, Zhang C, Wu K, Saddock ND, Jones JW, et al. *Z Metallkd* 2006;97:422.
- [4] Chang YA, Yang Y. Application of computational thermodynamics to rapidly determine multicomponent phase diagrams. In: Zhao J-C, editor. *Methods for phase diagram determination*. Oxford (OX5 1GB): Elsevier, Ltd.; 2007. p. 273.
- [5] Zhang F, Du Y, Oates WA, Chen S-L, Chang YA. *Acta Mater* 2003;51:207.
- [6] Zhu J, Zhang C, Cao W, Yang Y, Zhang F, Chen S-L, et al. *Acta Mater* 2008;57:202.
- [7] Hayashi S, Ford SI, Young DJ, Sorelet DJ, Besser MF, Gleeson B. *Acta Mater* 2005;53:3319.
- [8] Yang CN. *J Chem Phys* 1945;13:66.
- [9] Yang CN, Li Y. *Chin J Phys* 1947;7:59.
- [10] Li Y. *J Chem Phys* 1949;17:447.
- [11] Li Y. *Phys Rev* 1949;76:972.
- [12] Oates WA, Zhang F, Chen S-L, Chang YA. *Phys Rev* 1999;59B:11221.
- [13] Chang YA, Chen S-L, Zhang F, Yan X-Y, Xie F-Y, Schmid-Fetzer R, et al. *Prog Mater Sci* 2004;49:313.
- [14] Cao W, Chang YA, Zhu J, Chen S-L, Oates WA. *Acta Mater* 2005;53:331.

- [15] Cao W, Zhu J, Yang Y, Zhang F, Chen S-L, Oates WA, et al. *Acta Mater* 2005;53:4189.
- [16] Chang YA. *Mater Trans* 2006;37A:273;
Chang YA. *Mater Trans* 2006;37B:7.
- [17] Zhang C, Zhu J, Bengtson A, Morgan D, Zhang F, Cao W-S, et al. *Acta Mater* 2008;56:2576.
- [18] Zhang C, Zhu J, Bengtson A, Morgan D, Zhang F, Yang Y, et al. *Acta Mater* 2008;56:5796.
- [19] Zhu J. Thermodynamic description of multicomponent Ni-base superalloys containing Al, Cr, Ru and Pt: a computational thermodynamic approach coupled with experiments. PhD thesis, University of Wisconsin-Madison; 2008.
- [20] Neumann JP, Chang YA, Lee CM. *Acta Metall* 1976;24:593.
- [21] Chang YA, Neumann JP. In: Worrell WL, Rosenblatt GR, editors. *Progress in solid-state chemistry*, vol. 14. Oxford (UK): Pergamon Press; 1982. p. 221.
- [22] Hillert M, Staffanson LI. *Acta Chem Scand* 1970;24:3618.
- [23] Anderson JO, Guillermet AF, Hillert M, Jason B, Sundman B. *Acta Metall* 1986;34:437.
- [24] Bragg WL, Williams EJ. *Proc Roy Soc* 1934;A145:699.
- [25] Bragg WL, Williams EJ. *Proc Roy Soc* 1934;A151:540.
- [26] Bragg WL, Williams EJ. *Proc Roy Soc* 1935;A152:231.
- [27] Fowler RH. In: *Statistical mechanics*. Cambridge (England): Cambridge University Press; 1938. p. 162.
- [28] Oates WA, Wenzl H. *Scr Mater* 1996;35:623.
- [29] Redlich O, Kister A. *Ind Eng Chem* 1948;40:345.
- [30] Jiang C, Besser MF, Sordet DJ, Gleeson B. *Acta Mater* 2005;53:2101.
- [31] Jiang C, Sordet DJ, Gleeson B. *Phys Rev* 2005;72B:184203.
- [32] Dinsdale AT. *Calphad* 1991;15:317.
- [33] Pandat software for multi-component phase diagram calculation is available from CompuTherm LLC, 437 S. Yellowstone Drive, Suite 217, Madison (WI, USA); 2008.
- [34] Cao W, Chen S-L, Zhang F, Wu K, Yang Y, Chang YA, et al. *Calphad* 2009;33:328.
- [35] Castaing R. PhD thesis, University of Paris; 1951.
- [36] Armstrong JD. Lecture notes: quantitative microanalysis (CITZAF) using PC's. Lehigh University; 1996.
- [37] Carpenter P. Personal (email) communication; January 2, 2008.
- [38] Donovan JJ, Pingitore NE, Westphal W. *Microsc Microanal* 2003;9:202.
- [39] Copland E. *J Phase Equilib* 2007;28:38.
- [40] Flemings MC. *Solidification processing*. New York: McGraw-Hill; 1974.